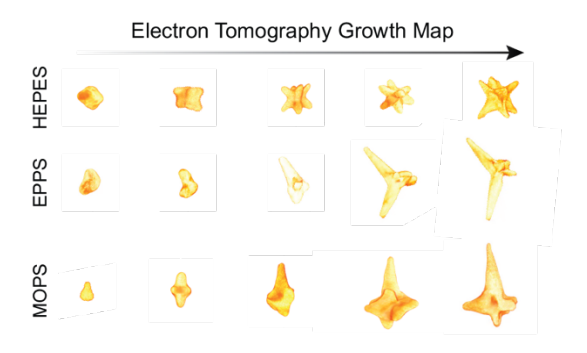
# Investigating Reaction Intermediates During the Seedless Growth of Gold Nanostars using Electron Tomography

Priscilla Choo<sup>†§</sup>, Daniel Arenas-Esteban<sup>‡, ||,§</sup>, Insub Jung<sup>†</sup>, Woo Je Chang<sup>⊥</sup>, Emily A. Weiss<sup>†</sup>, Sara Bals<sup>‡, ||,\*</sup>, and Teri W. Odom<sup>†,⊥,\*</sup>

†Department of Chemistry, Northwestern University, Evanston, Illinois 60208 ‡EMAT, University of Antwerp, Groenenborgerlaan 171, B-2020 Antwerp, Belgium "NANOlab Center of Excellence, University of Antwerp, Groenenborgerlaan 171, B-2020 Antwerp, Belgium

<sup>1</sup>Department of Materials Science and Engineering, Northwestern University, Evanston, Illinois 60208

# TOC:



**Keywords:** Gold nanostars, nanoparticle growth, multimode electron tomography, structural defects, seedless synthesis, nucleation, twinning

<sup>§</sup> These authors contributed equally to this work.

<sup>\*</sup>Corresponding Authors; E-mails: sara.bals@uantwerpen.be, todom@northwestern.edu

#### Abstract

Good's buffers can act both as nucleating and shape-directing agents during the synthesis of anisotropic gold nanostars (AuNS). Although different Good's buffers can produce AuNS shapes with branches that are oriented along specific crystallographic directions, the mechanism is not fully understood. This paper reports how an analysis of the intermediate structures during AuNS synthesis from HEPES, EPPS and MOPS Good's buffers can provide insight into the formation of seedless AuNS. Electron tomography of AuNS structures quenched at early times (minutes) was used to characterize the morphology of the incipient seeds, and later times were used to construct the growth maps. Through this approach, we identified how the crystallinity and shape of the first structures synthesized with different Good's buffers determines the final AuNS morphologies.

#### Introduction

Anisotropic gold nanoparticles (AuNPs) show shape-dependent optical properties that are driving a range of applications, from optical sensing to biomedical imaging to photocatalysis.<sup>1-5</sup> The preparation of anisotropic AuNPs with narrow shape distributions is important because of the strong correlation between morphology and optical properties.<sup>6, 7</sup> Although there are different approaches to synthesize anisotropic AuNPs,<sup>3, 8</sup> usually a desired NP shape has required the use of seed particles,<sup>9, 10</sup> where nucleation is followed by selective faceted growth.<sup>11, 12</sup> Previous work has shown that the crystal structure of seeds is maintained during growth<sup>13, 14</sup> and that seed size and shape influence the reaction kinetics and morphology of the final NP shape; however, tools to probe the evolution of NP morphology during the growth process have been limited.

X-ray and electron-based tools can indirectly investigate anisotropic NP growth. For example, time-resolved small angle x-ray scattering (SAXS) and x-ray near edge structure (XANES) have identified intermediate NP dimensions, polydispersity, and the different oxidation states of Au ions during the nucleation of Au nanorods and nanotriangles. <sup>15</sup> Electron paramagnetic resonance (EPR) spectroscopy revealed that different Good's buffers show different Au reduction behavior in the time-dependent changes in radical concentration during the growth of seedless gold nanostars. <sup>16</sup> *In situ* liquid transmission electron microscopy (TEM) can also track the growth of AuNPs in real time, but since nucleation is accompanied by radiolysis from the electron beam, the growth mechanism is affected by electron dose. <sup>17</sup> Electron tomography can directly characterize the 3D morphology of NPs, <sup>18</sup> including defects in seeds <sup>19</sup> as well as provide visualization of how anisotropic NP shapes evolve. <sup>20</sup>

Gold nanostars (AuNS) are interesting because of their 3D anisotropic structure, branch length-dependent optical properties, and high absorption-to-scattering ratios. <sup>21-24</sup> Because of the increased electromagnetic field enhancement at the tips and localized surface plasmon resonance within the

near-IR window, AuNS are model nanostructures for surface-enhanced Raman spectroscopy, biosensing, and photothermal applications. 25-27 Their high surface areas and functionalization with thiolated molecules has enabled their use in catalysis and drug delivery.<sup>28</sup> The typical synthesis of AuNS involves seeded overgrowth, where branches are grown on different sizes of Au NP seeds using shape-directing agents to grow large numbers of branches.<sup>29, 30</sup> AuNS can also be prepared in a one-pot, seedless method using biocompatible Good's buffers that act as both nucleating and shape-directing agents; the size, shape, and branch lengths can be readily tuned by changing the reaction parameters. <sup>31, 32</sup> Good's buffers represent a class of twenty zwitterionic buffering agents used in biological applications due to their high water solubility, low cell membrane permeability, and low optical absorption from the UV to visible wavelength range.<sup>33</sup> Recently, Good's buffers with morpholine and piperazine moieties have been used as nucleating and shape-directing agents to synthesize AuNS with tailorable branch lengths and tunable optical properties.<sup>31</sup> Although high resolution TEM can determine the crystalline growth directions of AuNS branches in the final structures, <sup>32</sup> visualization of how the earliest formed AuNS nanostructures affects the intermediate and final AuNS morphologies has not been studied in detail.

Here we show how the growth mechanism of seedless AuNS synthesized using three different Good's buffers can be characterized by electron tomography. We obtained 3D reconstructions for AuNS synthesized by HEPES (2-[4-(2-hydroxyethyl)piperazine-1-yl]ethanesulfonic acid), EPPS (4-(2-hydroxyethyl)-1-piperazinepropanesulfonic acid), and MOPS (3-morpholinopropane-1-sulfonic acid) and HAuCl<sub>4</sub>. AuNS reactions were quenched at different time points, and growth maps for the most dominant AuNS shapes from each buffer were compared. 2D and 3D electron microscopy revealed the configuration of structural defects in the intermediate structures that correspond to single-crystalline, penta-twinned, and multi-twinned seeds for HEPES, EPPS, and

MOPS AuNS, respectively. Our results suggest that the initial nucleated structure is critical in directing the final structure of seedless AuNS synthesized with Good's buffers.

# **Results and Discussion**

Low-magnification TEM images show how AuNS morphology changed over time for each Good's buffer (**Figure 1**). The growth reactions of HEPES, EPPS, MOPS AuNS were quenched at 4, 6, 10, 20, 30 min, and 1 h using thiolated polyethylene glycol (mPEG-thiol, MW 5000) according to our previous protocol (**Figure S1**). <sup>16</sup> For all buffers, near-spherical structures formed at the initial synthetic time points. For HEPES AuNS, incipient branches were observed after 6 min (**Figure 1a**), while for EPPS and MOPS AuNS, distinct branches emerged only after 20 min (**Figures 1b-c**). After 10 min, most HEPES AuNS adopted a cubic-like shape, where eight short branches are oriented toward the vertices of a cube. For EPPS and MOPS AuNS, one to four long

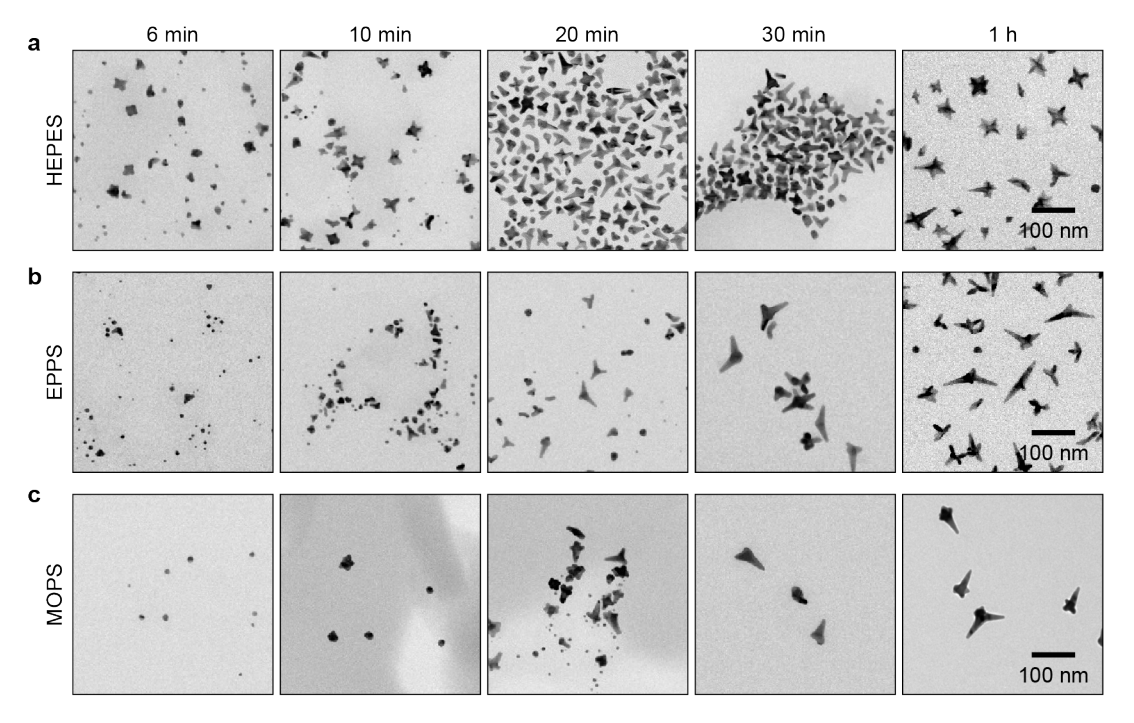
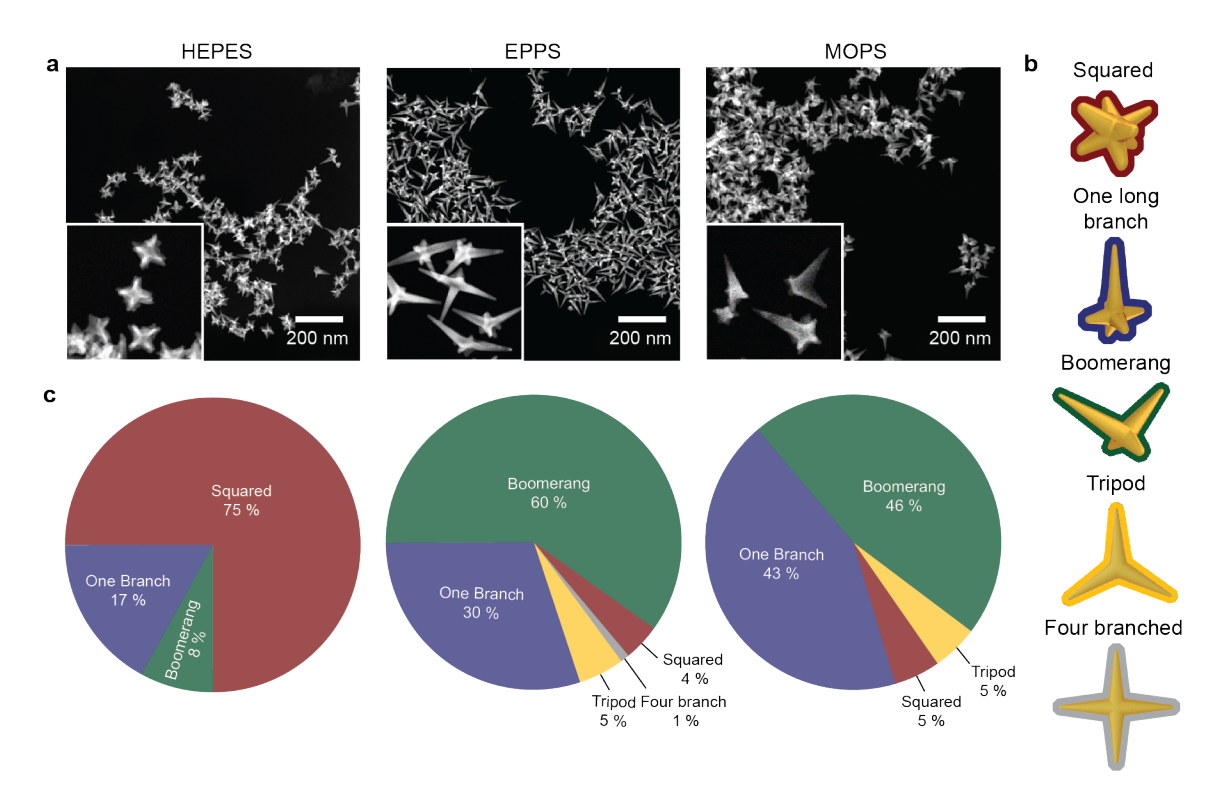


Figure 1. 2D TEM images of quenched AuNS at different time points. (a) HEPES AuNS, (b) EPPS AuNS, (c) MOPS AuNS, respectively.

branches were observed after 1 h, which confirmed that the growth kinetics of AuNS from different buffers are distinct.<sup>16, 34</sup>

As an additional confirmation that the AuNS branches increased in length with reaction time, we correlated the structural shapes determined by TEM with the optical properties of the growth solution at the same time points (**Figure S2**). The localized surface plasmon (LSP) resonance wavelength shifted to longer wavelengths as the branch lengths increased. For HEPES AuNS, redshifting of the resonance wavelength was gradual and became more pronounced after 10 min; for EPPS and MOPS AuNS, red-shifting of the LSP started at 20 min and became more noticeable between 30 min to 1 h, which agrees with lengthening of branches during this period.<sup>32</sup>

Since AuNS seedless synthesis is at room temperature and involves only two reagents, the gold salt (HAuCl<sub>4</sub>) and the Good's buffer, the final AuNS products have various sizes and shapes. We focused on the most dominant morphologies from each Good's buffer for growth map construction and used density gradient centrifugation to select specific AuNS populations<sup>34</sup> (**Figure S3**). **Figure 2** shows high angular annular dark field scanning transmission electron microscopy (HAADF-STEM) images of the different AuNS used in our statistical analysis. Based on these 2D projection images, we hypothesize that there are five different final shapes from the three Good's buffers: squared, one long branch, boomerang, tripod, and four branched (which can be tetrahedron or flat star shaped) (**Figure 2b**). The population distribution was carried out by analyzing 100 particles for each buffer from low magnification HAADF-STEM images. For HEPES AuNS, the squared shape was the most dominant (75%), and the one long branch (17%) and boomerang shape (9%) were of minor populations. For EPPS AuNS, the boomerang shape was the most dominant (60%),



**Figure 2. Population distribution of fully grown AuNS.** (a) HAADF-STEM images of HEPES, EPPS, MOPS AuNS with insets showing zoomed in images of the particles. Insets are 200 nm by 200 nm. (b) Schemes representing dominant shapes. (c) Pie charts showing different population distribution of shapes of HEPES, EPPS, MOPS AuNS.

AuNS, the boomerang shape (46%) and the one long branch (43%) were equally dominant, followed by the tripod (5%) and squared (5%) morphologies (**Figure 2c**).

Growth maps of the dominant AuNS shapes for each buffer were constructed by performing electron tomography for particles quenched at different time points (6, 10, 20, 30 min, and 1 h) (**Figure 3**). The squared shape was selected for HEPES AuNS (**Movie S1**); the boomerang shape for EPPS AuNS (**Movie S2**); and both boomerang shape and one long branch for MOPS AuNS (**Movies S3**, **S4**). All tomography series were reconstructed using the Simultaneous Iterative Reconstruction Technique (SIRT) algorithm.<sup>35</sup> As determined from the growth maps, the initial

particle shape after 6 min directs the morphology of the final structures. HEPES AuNS show

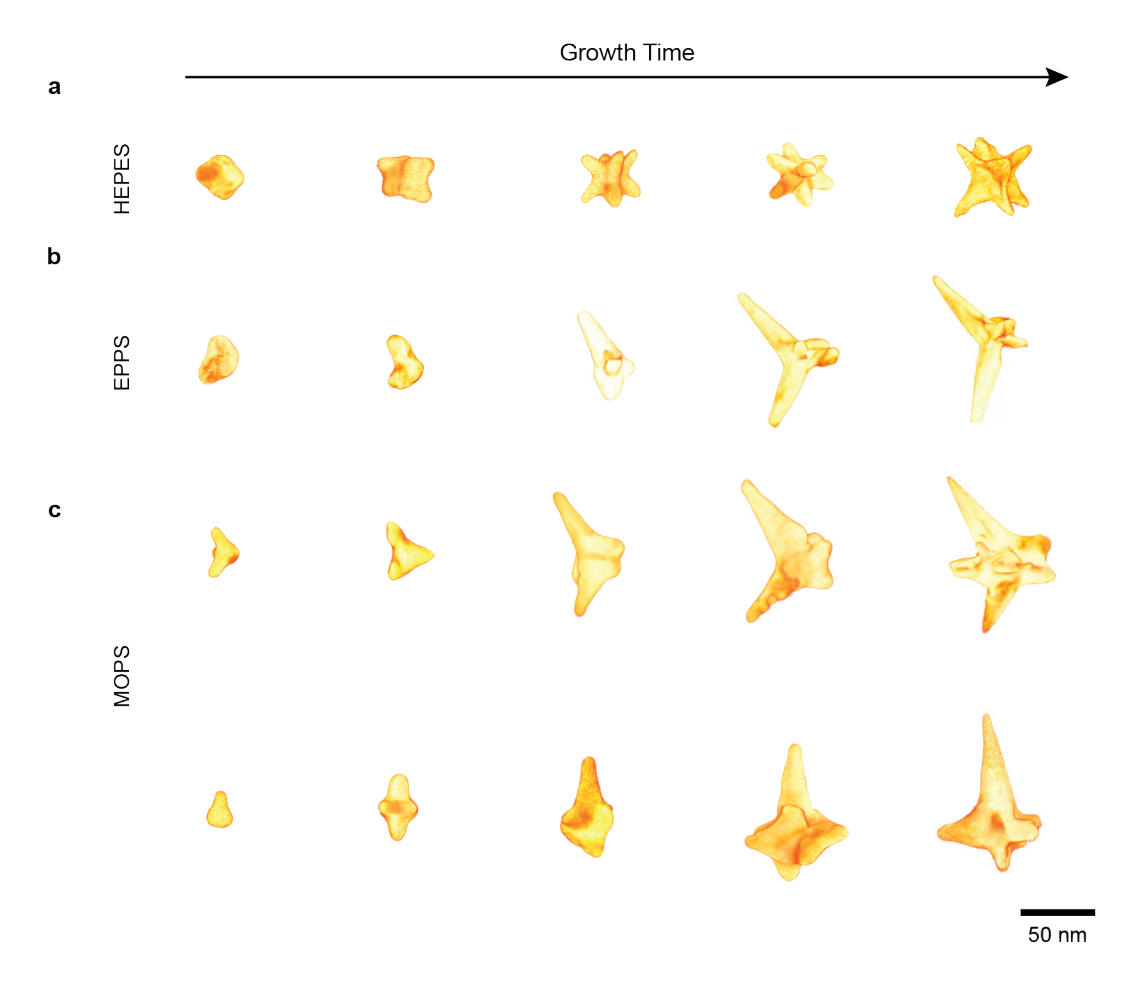


**Figure 3. 3D tomography images of (a)** HEPES AuNS, **(b)** EPPS AuNS, and **(c)** MOPS AuNS at 6, 10, 20, 30 min, and 1 h.

relatively isotropic seeds that result in the squared morphology with 8 branches, while EPPS AuNS grow from seeds that are elongated with two branches at an angle of ~160°. Most boomerang-shaped EPPS AuNS only had three short branches. In general, MOPS AuNS showed higher heterogeneity of shape and size of the initial structures, and the intermediate structures also had distorted shapes and more branches. For MOPS AuNS that grew into boomerang shapes, compared to EPPS AuNS, the particles had > 10 nm larger core sizes and sharper branch tips that tapered down to 2-3 nm in diameter. These discrepancies indicate that although the final shapes are similar,

there must be internal differences that represent how the gold precursor interacts with the buffers during reduction and adsorption to the particle surface.

To identify the presence of defects along specific directions, we used low-magnification low angle annular darkfield scanning transmission electron microscopy (LAADF-STEM), a technique that yields diffraction contrast.  $^{19,20}$  For each Good's buffer, images for AuNS at early stages were recorded over a tilt range of  $\pm 50^{\circ}$  and with a tilt increment of  $5^{\circ}$ . Although HEPES AuNS seeds

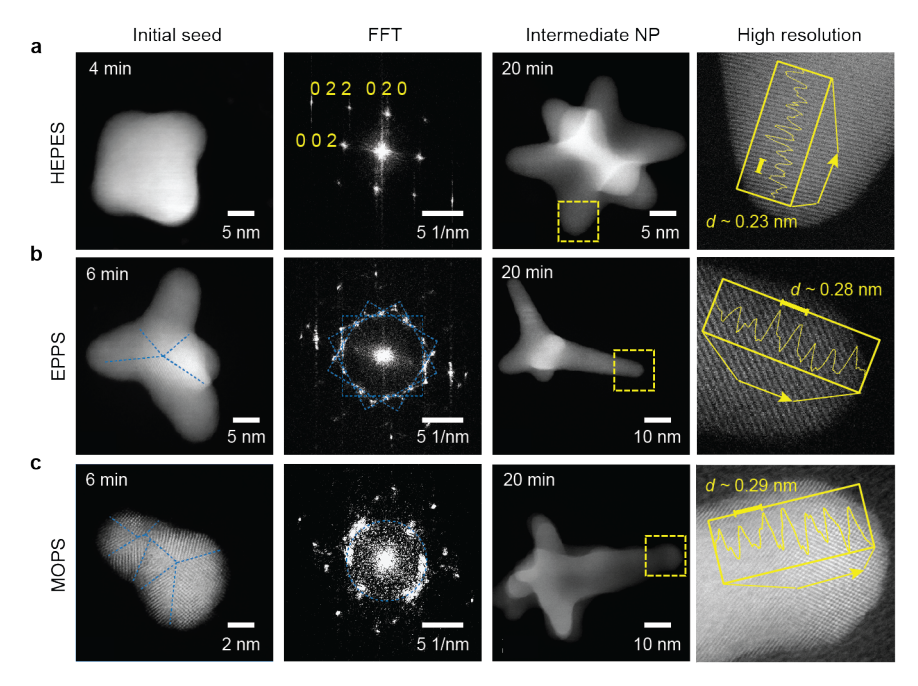


**Figure 4. Seeds crystallinity and branches growth direction of HEPES, EPPS, MOPS AuNS. (a)** HEPES AuNS initial seed quenched at 4 min and its corresponding FFT show a single-crystal diffraction pattern. Intermediate AuNS quenched at 20 min and a high resolution HAADF-STEM image of a branch where an intensity line profile along the growth direction is along [111] ( $d \sim 0.23$  nm). **(b)** EPPS AuNS initial seed quenched at 6 min showing few twin planes converging to the same point at the center of the particle and its corresponding FFT diffraction pattern marked by blue dotted lines. Intermediate AuNS quenched at 20 min and a high resolution HAADF-STEM image of a branch where an intensity line profile along the growth direction is along [110] ( $d \sim 0.28$  nm). **(c)** MOPS AuNS initial seed quenched at 6 min and its FFT showing a multi twinned diffraction pattern marked by blue dotted lines. Intermediate AuNS quenched at 20 min and a high resolution HAADF-STEM image of a branch where an intensity line profile along the growth direction is along [110] ( $d \sim 0.29$  nm).

are single crystalline (**Figure S4**), EPPS AuNS show a mix of penta-twinned seeds and multitwinned seeds (**Figure S5**), and MOPS AuNS mostly show multi-twinned seeds (**Figure S6**). These observations were further confirmed by high resolution HAADF-STEM and fast Fourier transform (FFT) images (**Figure 4**). From the FFT analysis of the initial seeds, the single-crystalline nature of HEPES AuNS seeds was clear (**Figure 4a**), whereas EPPS AuNS (**Figure 4b**) and MOPS AuNS (**Figure 4c**) had initial particles with few and multiple twinned planes, respectively. High resolution HAADF-STEM images of AuNS quenched at longer times showed intermediate structures with preferential crystallographic growth directions for the branches of each morphology. HEPES AuNS branches grow along the [111] direction with  $d \sim 0.23$  nm between lattice planes, while MOPS AuNS and EPPS AuNS had primary growth directions along [110] with  $d \sim 0.28$  nm between lattice planes, as expected.<sup>32</sup>

Although twin planes are observed in both the initial structures of EPPS and MOPS AuNS, the location and number of defects within the seeds are different, which likely explains why the final morphologies of the two AuNS have different numbers of branches. We used multimode electron tomography, a combination of HAADF-STEM and LAAD-STEM tomography, to colocalize the defects and the seed structure (**Figure 5**). The main challenge is that when the acquisition angle is reduced from the HAADF to the LAADF regime, the projection requirement for tomography starts to break down since diffraction contrast becomes increasingly dominant. Reconstruction performed by LAADF-STEM can therefore lead to lower-quality reconstructions of nanoparticle morphology. To overcome this problem, we selected an optimal value for the collection angle as a compromise between optimal contrast for visualizing defects and fulfilment of the projection requirement. HAADF-STEM provides the NP shape from the 3D reconstruction, which is based on Z-contrast, and LAADF-STEM allows for defect contrast analysis. Hence, using different ADF

detectors, simultaneous 3D reconstruction of particle shape and twining defects is possible. 19, 20

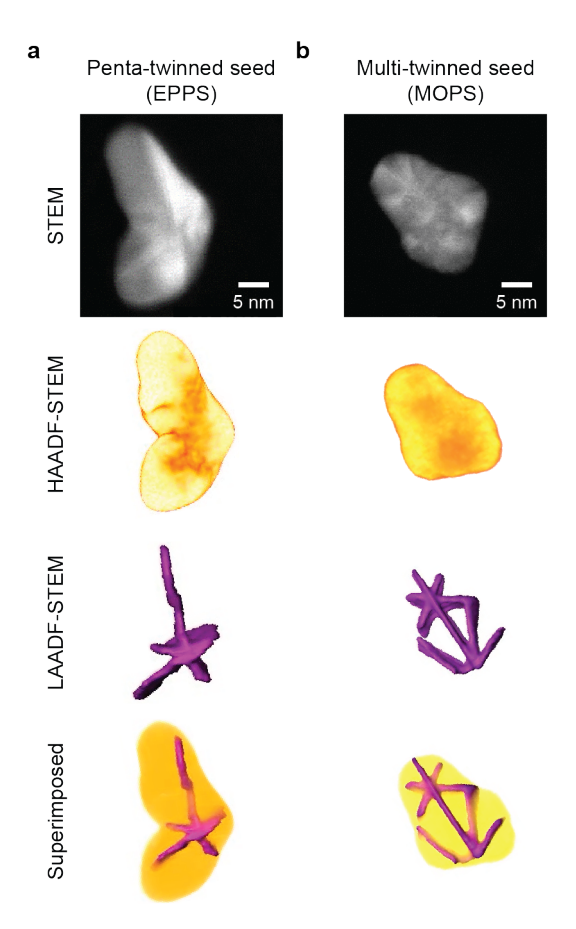


Figure 5. Characterizing structural defects of penta-twinned and multi-twinned seeds. STEM, HAADF-STEM, LAADF-STEM, and superimposed images showing twin boundaries of (a) EPPS AuNS quenched at 6 min and (b) MOPS AuNS quenched at 6 min. the

The HAADF-STEM tomography of EPPS AuNS seed quenched at 6 min resembled the final morphology of the boomerang shaped seed (**Figure 5a, second row**), while the LAADF-STEM showed 5 lines protruding out of the particle core (**Figure 5a, third row**), indicating a clear pentatwinning behavior (**Movie S5**). The superimposed image colocalized the defects with respect to the seed, with two lines extending along the growth direction of the long branches (**Figure 5a,** fourth row). In contrast, HAADF-STEM tomography of MOPS AuNS seed did not show a specific

morphology (**Figure 5b**, second row), while the LAADF-STEM showed multiple random twinning (**Figure 5a**, third row). The superimposed image that overlays defects with respect to the seed shows that MOPS AuNS seeds have complex twinning behavior (**Movie S6**). These differences in seed structure explain how boomerang-shaped AuNS for both buffers can be differentiated from each other, where the boomerang-shaped AuNS from MOPS are thicker in body size compared to those obtained with EPPS.

To investigate if this difference in crystallinity of the initial structures can be attributed to differences between the reduction potential of the buffers during the synthesis, we compared cyclic voltammograms (CVs) of the three different buffers after adding HAuCl<sub>4</sub> (**Figure S7**). The CV of HAuCl<sub>4</sub> in HEPES and EPPS buffers showed relatively weak responses, while MOPS buffer showed peaks corresponding to three reversible one-electron reductions: Au<sup>3+</sup>/Au<sup>2+</sup> (E<sub>1/2</sub>= -0.45 V vs. Ag/AgCl), Au<sup>2+</sup>/Au<sup>+</sup> (-0.54 V), and Au<sup>+</sup>/Au<sup>0</sup> (-0.71 V). We attribute differences in the CV spectra among the different buffers from: (1) the coordination of Au<sup>3+</sup> with HEPES and EPPS shielding the electron transfer process more than MOPS; or (2) the presence of two tertiary amine groups allowing faster coordination of Au ions to the piperazine ring for HEPES and EPPS, while the single tertiary amine in the morpholine ring of MOPS leading to slower changes in the oxidation state of Au ion as the number of coordination sites for Au<sup>3+</sup> decreased.

# **Conclusions**

In summary, we used a correlative approach to determine the seedless growth mechanism of AuNS synthesized with three Good's buffers: HEPES, EPPS, and MOPS. Using 2D (S)TEM, we quantified the population distribution of different shapes of AuNS synthesized with each buffer and identified the most dominant structure. Using electron tomography, we visualized the 3D structure of AuNS quenched at different time points and constructed the growth map for the most

dominant AuNS morphology synthesized from the different buffers. Furthermore, we found that HEPES AuNS were single crystalline, EPPS AuNS had a penta-twinned structure, and MOPS AuNS had multiple randomly ordered twin planes. Therefore, our studies demonstrate that small differences in the molecular structure of Good's buffers can lead to large differences in the initial nucleation step of gold precursors, and ultimately produce AuNS with different shapes, sizes, and branch growth direction. This study on the relationship between the initial structures formed and the AuNS final structures suggests that electron tomography is a powerful tool that can achieve mechanistic understanding of the anisotropic growth of plasmonic nanostructures.

#### **Experimental Section**

# Synthesis of seedless AuNS

Three Good's buffers were used: 4-(2-hydroxyethyl)piperazine-1-ethanesulfonic acid (HEPES buffer, Sigma-Aldrich), 4-(2-hydroxyethyl)-1piperazinepropanesulfonic acid (EPPS buffer, Sigma-Aldrich), and 3-(N-morpholino)propanesulfonic acid (MOPS buffer, Sigma-Aldrich). The 1-M stock solutions were made by dissolving the buffer salt in Millipore water (18.2  $M\Omega$ ·cm) using a stir bar to ensure thorough mixing. The pH of the buffer solutions was measured using a Thermo Scientific pH meter while being adjusted using NaOH pellets. AuNS were synthesized by adding 100  $\mu$ L of 0.2 mM (final concentration) gold(III) chloride trihydrate (HAuCl4; Sigma-Aldrich) to 110 mM, 500 mM, 180 mM concentrations of HEPES, EPPS, MOPS buffers, respectively to make a final volume of 20 mL. Each solution was vortexed at max power for 1 min to allow for thorough mixing and kept in the dark to allow for nucleation.

# Quenching of AuNS growth by mPEG-SH

After 1 min of vortexing, the particles were allowed to nucleate. At different time points, 900  $\mu$ L of each solution was withdrawn into an Eppendorf tube, and 100  $\mu$ L MW 5000 mPEG-SH was

added quickly. The solution was allowed for agitation on the shaker at 700 rpm for 30 s - 1 min to allow for mPEG-SH to attach to gold surface. Particles were centrifuged twice at 7000 rpm for 10 minutes to remove excess mPEG. The final concentration of mPEG-thiol was 33  $\mu$ M.

# **Electron microscopy characterization**

Transmission electron microscopy (TEM) images were obtained using BioCryo Hitachi HD2300 STEM operated at 200 kV. Scanning transmission electron microscopy (STEM) images were obtained using an aberration corrected "cubed" Thermo Fisher Scientific Titan 60–300 electron microscope operated at 300 kV. Samples were prepared by dropcasting the corresponding nanoparticle solution on carbon-coated copper grids. Tomography series were acquired using the Fischione model 2020 single-tilt tomography holder over a tilt range from –75° to +75°, with tilt increments of 3°. For HAADF-STEM and LAADF-STEM multimode electron tomography, tilt series were simultaneously acquired using two annular detectors with acquisition angles ranging from 13 to 115 mrad for LAADF-STEM and from 115 to 157 mrad for HAADF-STEM. The reconstruction of the tilt series was performed using the Astra Toolbox 1.8 for MATLAB 2018a.<sup>36</sup>

# Cyclic voltammetry of Good's buffers upon gold addition

Cyclic voltammograms of HEPES, EPPS and MOPS buffers (110 mM, 500 mM, 180 mM, respectively) were obtained before and after HAuCl<sub>4</sub> addition from a pre-synthesized 40 mM stock solution (0.2 mM final concentration). The scan rate was 0.1 V/s, and the scanning window was from -1 V to 0 V. The reference electrode was Ag/AgCl, counter electrode was Pt, and a glassy carbon cell was used.

#### ASSOCIATED CONTENT

*Supporting Information available*: The Supporting Information is available free of charge via the Internet at http://pubs.acs.org.

UV-Vis spectra of AuNS during growth; 2D TEM images of AuNS; cyclic voltammograms of HEPES, EPPS, MOPS after gold addition.

Supporting movies S1, S2 are electron tomography videos of HEPES and EPPS AuNS. Movies S3, S4 are electron tomography videos of MOPS AuNS. Movies S5, S6 show multimode electron tomograph videos of EPPS AuNS, and MOPS AuNS seed, respectively.

#### **AUTHOR INFORMATION**

# **Corresponding authors**

**Teri W. Odom** – Department of Chemistry, Northwestern University, 2145 Sheridan Road, Evanston, Illinois 60208, United states. E-mail: <a href="mailto:todom@northwestern.edu">todom@northwestern.edu</a>

Sara Bals – EMAT and NANOlab Center of Excellence, Univ. of Antwerp, Groenenborgerlaan 171, Antwerp 2020, Belgium E-mail: <a href="mailto:sara.bals@uantwerpen.be">sara.bals@uantwerpen.be</a>

#### **Authors**

**Priscilla Choo** – Department of Chemistry, Northwestern University, 2145 Sheridan Road, Evanston, Illinois 60208, United states

**Daniel Arenas Esteban** – EMAT and NANOlab Center of Excellence, Univ. of Antwerp, Groenenborgerlaan 171, Antwerp 2020, Belgium

**Insub Jung** – Department of Chemistry, Northwestern University, 2145 Sheridan Road, Evanston, Illinois 60208, United States

**Woo Je Chang** – Department of Materials Science and Engineering, Northwestern University, 2145 Sheridan Road, Evanston, Illinois 60208, United States

Emily A. Weiss – Department of Chemistry, Northwestern University, 2145 Sheridan Road, Evanston, Illinois 60208, United States

**ORCID** 

Priscilla Choo: 0000-0003-1546-2390

Daniel A. Esteban: 0000-0002-5626-9848

Insub Jung: 000-0003-0827-9280

Woo Je Chang: 0000-0003-0796-9271

Emily A. Weiss: 0000-0001-5834-463X

Sara Bals: 0000-0002-4249-8017

Teri W. Odom: 0000-0002-8490-292X

**Author Contributions** 

T.W.O and S.B. conceived the idea of investigating seedless growth of AuNS using electron

tomography. P.C. and I.J. synthesized, sorted, and refined AuNS of interest. D.A.E. collected

electron tomography images and videos. P.C. and W.C. obtained

Acknowledgments

This work was supported by the National Science Foundation (NSF) under award NSF CHE-

1808502 (P.C., I.J.). This work made use of the EPIC facility of Northwestern University's

NUANCE Center, which has received support from the SHyNE Resource (NSF ECCS-2025633),

the IIN, and Northwestern's MRSEC program (NSF DMR-1720139).

**Notes** 

The authors declare no competing financial interest.

16

#### References

- 1. Hua, Y.; Chandra, K.; Dam, D. H.; Wiederrecht, G. P.; Odom, T. W., Shape-Dependent Nonlinear Optical Properties of Anisotropic Gold Nanoparticles. *J Phys Chem Lett* **2015**, *6* (24), 4904-4908.
- 2. Huang, X.; Jain, P. K.; El-Sayed, I. H.; El-Sayed, M. A., Gold Nanoparticles: Interesting Optical Properties and Recent Applications in Cancer Diagnostics and Therapy. *Nanomedicine* (Lond) **2007**, *2* (5), 681-693.
- 3. Yang, L.; Zhou, Z.; Song, J.; Chen, X., Anisotropic Nanomaterials for Shape-Dependent Physicochemical and Biomedical Applications. *Chem. Soc. Rev.* **2019**, *48* (19), 5140-5176.
- 4. Jauffred, L.; Samadi, A.; Klingberg, H.; Bendix, P. M.; Oddershede, L. B., Plasmonic Heating of Nanostructures. *Chem Rev* **2019**, *119* (13), 8087-8130.
- 5. Reguera, J.; Langer, J.; Jimenez de Aberasturi, D.; Liz-Marzan, L. M., Anisotropic metal nanoparticles for surface enhanced Raman scattering. *Chem Soc Rev* **2017**, *46* (13), 3866-3885.
- 6. Nehl, C. L.; Liao, H.; Hafner, J. H., Optical Properties of Star-Shaped Gold Nanoparticles. *Nano Lett* **2006**, *6* (4), 683-8.
- 7. Kelly, K. L., Coronado, E., Zhao, L.L., Schatz., G.C., The Optical Properties of Metal Nanoparticles: The Influence of Size, Shape, and Dielectric Environment. *J. Phys. Chem. B.* **2002**, *107* (3), 668-677.
- 8. Burrows, N. D.; Harvey, S.; Idesis, F. A.; Murphy, C. J., Understanding the Seed-Mediated Growth of Gold Nanorods through a Fractional Factorial Design of Experiments. *Langmuir* **2017**, *33* (8), 1891-1907.
- 9. Lohse, S., Murphy, C.J., The Quest for Shape Control: A History of Gold Nanorod Synthesis. *Chem. Mater.* **2013**, *25* (8), 1250-1261.
- 10. Pearce, A. K., Wilks, T.R., Arno, M.C., O'Reilly, R.K., Synthesis and Applications of Anisotropic Nanoparticles with Precisely Defined Dimensions. *Nat. Rev. Chem.* **2021**, *5*, 21-45.
- 11. Ziegler, C., Eychmüller, A., Seeded Growth Synthesis of Uniform Gold Nanoparticles with Diameters of 15–300 nm. *J. Phys. Chem. C* **2011**, *115* (11), 4502-4506.
- 12. Hinman, J. G.; Stork, A. J.; Varnell, J. A.; Gewirth, A. A.; Murphy, C. J., Seed Mediated Growth of Gold Nanorods: Towards Nanorod Matryoshkas. *Faraday Discuss.* **2016**, *191*, 9-33.
- 13. Liu, M.; Guyot-Sionnest, P., Mechanism of Silver(I)-Assisted Growth of Gold Nanorods and Bipyramids. *J. Phys. Chem. B* **2005**, *109* (47), 22192-200.
- 14. Grzelczak, M.; Perez-Juste, J.; Mulvaney, P.; Liz-Marzan, L. M., Shape Control in Gold Nanoparticle Synthesis. *Chem Soc Rev* **2008**, *37* (9), 1783-91.
- 15. Hubert, F., Testard, F., Thill, A., Kong, Q., Tache, O., Spalla, O., Growth and Overgrowth of Concentrated Gold Nanorods: Time Resolved SAXS and XANES. *Cryst. Growth Des.* **2012**, *12*, 1548-1555.
- 16. Chandra, K.; Rugg, B. K.; Ratner, M. A.; Wasielewski, M. R.; Odom, T. W., Detecting and Visualizing Reaction Intermediates of Anisotropic Nanoparticle Growth. *J Am Chem Soc* **2018**, *140* (9), 3219-3222.
- 17. Ahmad, N.; Wang, G.; Nelayah, J.; Ricolleau, C.; Alloyeau, D., Exploring the Formation of Symmetric Gold Nanostars by Liquid-Cell Transmission Electron Microscopy. *Nano Lett.* **2017**, *17* (7), 4194-4201.
- 18. Albrecht, W.; Bladt, E.; Vanrompay, H.; Smith, J. D.; Skrabalak, S. E.; Bals, S., Thermal Stability of Gold/Palladium Octopods Studied in Situ in 3D: Understanding Design Rules for Thermally Stable Metal Nanoparticles. *ACS Nano* **2019**, *13* (6), 6522-6530.

- 19. Winckelmans, N.; Altantzis, T.; Grzelczak, M.; Sanchez-Iglesias, A.; Liz-Marzan, L. M.; Bals, S., Multimode Electron Tomography as a Tool to Characterize the Internal Structure and Morphology of Gold Nanoparticles. *J. Phys. Chem. C* **2018**, *122* (25), 13522-13528.
- 20. Smith, J. D.; Bladt, E.; Burkhart, J. A. C.; Winckelmans, N.; Koczkur, K. M.; Ashberry, H. M.; Bals, S.; Skrabalak, S. E., Defect-Directed Growth of Symmetrically Branched Metal Nanocrystals. *Angew Chem Int Ed Engl* **2020**, *59* (2), 943-950.
- 21. Yuan, H.; Khoury, C. G.; Hwang, H.; Wilson, C. M.; Grant, G. A.; Vo-Dinh, T., Gold Nanostars: Surfactant-Free Synthesis, 3D Modelling, and Two-photon Photoluminescence Imaging. *Nanotechnology* **2012**, *23* (7), 075102.
- 22. Yuan, H.; Fales, A. M.; Vo-Dinh, T., TAT Peptide-functionalized Gold Nanostars: Enhanced Intracellular Delivery and Efficient NIR Photothermal Therapy using Ultralow Irradiance. *J Am Chem Soc* **2012**, *134* (28), 11358-61.
- 23. Yuan, H.; Khoury, C. G.; Wilson, C. M.; Grant, G. A.; Bennett, A. J.; Vo-Dinh, T., In Vivo Particle Tracking and Photothermal Ablation using Plasmon-Resonant Gold Nanostars. *Nanomedicine* **2012**, *8* (8), 1355-63.
- 24. Tsoulos, T. V., Han, L., Weir, J., Xin, H.L, Fabris, L., A Closer Look at the Physical and Optical Properties of Gold Nanostars: an Experimental and Computational Study. *Nanoscale* **2016**, *9*, 3766-3773.
- 25. Atta, S., Tsoulos, T.V., Fabris, L., Shaping Gold Nanostar Electric Fields for Surface-Enhanced Raman Spectroscopy Enhancement via Silica Coating and Selective Etching. *J Phys Chem C* **2016**, (37), 20749-20758.
- 26. Dondapati, S. K.; Sau, T. K.; Hrelescu, C.; Klar, T. A.; Stefani, F. D.; Feldmann, J., Label-Free Biosensing Based on Single Gold Nanostars as Plasmonic Transducers. *ACS Nano* **2010**, *4* (11), 6318-22.
- 27. Dam, D. H.; Culver, K. S.; Kandela, I.; Lee, R. C.; Chandra, K.; Lee, H.; Mantis, C.; Ugolkov, A.; Mazar, A. P.; Odom, T. W., Biodistribution and In Vivo Toxicity of Aptamer-Loaded Gold Nanostars. *Nanomedicine* **2015**, *11* (3), 671-9.
- 28. Dam, D. H.; Lee, J. H.; Sisco, P. N.; Co, D. T.; Zhang, M.; Wasielewski, M. R.; Odom, T. W., Direct Observation of Nanoparticle-Cancer Cell Nucleus Interactions. *ACS Nano* **2012**, *6* (4), 3318-26.
- 29. Senthil Kumar, P.; Pastoriza-Santos, I.; Rodriguez-Gonzalez, B.; Javier Garcia de Abajo, F.; Liz-Marzan, L. M., High-yield Synthesis and Optical Response of Gold Nanostars. *Nanotechnology* **2008**, *19* (1), 015606.
- 30. Pu, Y.; Zhao, Y.; Zheng, P.; Li, M., Elucidating the Growth Mechanism of Plasmonic Gold Nanostars with Tunable Optical and Photothermal Properties. *Inorg Chem* **2018**, *57* (14), 8599-8607.
- 31. Xie, J., Lee, J.Y., Wang, D.I.C., Seedless, surfactantless, high-yield synthesis of branchednanocrystals in HEPES buffer solution. *Chem Mater* **2007**, *19*, 2823-2839.
- 32. Chandra, K.; Culver, K. S. B.; Werner, S. E.; Lee, R. C.; Odom, T. W., Manipulating the Anisotropic Structure of Gold Nanostars using Good's Buffers. *Chemistry of Materials* **2016**, *28* (18), 6763-6769.
- 33. Taha, M.; FA, E. S.; Quental, M. V.; Ventura, S. P.; Freire, M. G.; Coutinho, J. A., Good's Buffers as a Basis for Developing Self-Buffering and Biocompatible Ionic Liquids for Biological Research. *Green Chem* **2014**, *16* (6), 3149-3159.
- 34. Chandra, K.; Kumar, V.; Werner, S. E.; Odom, T. W., Separation of Stabilized MOPS Gold Nanostars by Density Gradient Centrifugation. *ACS Omega* **2017**, *2* (8), 4878-4884.

- 35. Goris, B.; Roelandts, T.; Batenburg, K. J.; Heidari Mezerji, H.; Bals, S., Advanced Reconstruction Algorithms for Electron Tomography: From Comparison to Combination. *Ultramicroscopy* **2013**, *127*, 40-7.
- 36. van Aarle, W.; Palenstijn, W. J.; Cant, J.; Janssens, E.; Bleichrodt, F.; Dabravolski, A.; De Beenhouwer, J.; Joost Batenburg, K.; Sijbers, J., Fast and Flexible X-ray Tomography using the ASTRA Toolbox. *Opt Express* **2016**, *24* (22), 25129-25147.